

A distinct role for $Lgr5^+$ stem cells in primary and metastatic colon cancer

Felipe de Sousa e Melo¹, Antonina V. Kurtova¹, Jonathan M. Harnoss², Noelyn Kljavin¹, Joerg D. Hoeck¹, Jeffrey Hung³, Jeffrey Eastham Anderson³, Elaine E. Storm¹, Zora Modrusan⁴, Hartmut Koeppen³, Gerrit J. P. Dijkgraaf¹, Robert Piskol⁵ & Frederic J. de Sauvage¹

Cancer stem cells (CSCs) have been hypothesized to represent the driving force behind tumour progression and metastasis, making them attractive cancer targets. However, conclusive experimental evidence for their functional relevance is still lacking for most malignancies. Here we show that the leucine-rich repeat-containing G-protein-coupled receptor 5 ($Lgr5$) identifies intestinal CSCs in mouse tumours engineered to recapitulate the clinical progression of human colorectal cancer. We demonstrate that selective $Lgr5^+$ cell ablation restricts primary tumour growth, but does not result in tumour regression. Instead, tumours are maintained by proliferative $Lgr5^-$ cells that continuously attempt to replenish the $Lgr5^+$ CSC pool, leading to rapid re-initiation of tumour growth upon treatment cessation. Notably, CSCs are critical for the formation and maintenance of liver metastasis derived from colorectal cancers. Together, our data highlight distinct CSC dependencies for primary versus metastatic tumour growth, and suggest that targeting CSCs may represent a therapeutic opportunity for managing metastatic disease.

Colorectal cancer is a leading cause of cancer-related death¹ and progresses owing to the sequential acquisition of specific genetic alterations, including functional loss of tumour suppressors such as *APC*, *TP53* and *SMAD4*, as well as activating mutations in oncogenes such as *KRAS*². Only a subset of cells within these tumours has tumorigenic potential^{3,4}, suggesting a hierarchical organization. These cells, referred to as CSCs, are thought to represent the clonogenic core of the tumour and can be identified by specific markers, including leucine-rich repeat-containing G-protein-coupled receptor 5 ($LGR5$)^{5–8}. Targeting CSCs is predicted to have widespread clinical implications, since it is assumed that these cells are involved in tumour progression and metastatic dissemination⁹. Although CSCs have been identified in various tumour types^{10,11}, their clinical relevance remains unclear and still awaits the development of relevant pre-clinical experimental systems in which the selective depletion of CSCs can be achieved^{12,13}.

Modelling colorectal cancer progression

To investigate the functional role of CSCs in colorectal cancer initiation, growth and metastasis, we combined the *Apc*^{min/+};*Kras*^{LSL-G12D/+};*Vil1*^{Cre} (AKV) model of intestinal tumorigenesis^{6,14} with the *Lgr5*^{DTR/eGFP} allele¹⁵. The resulting *Apc*^{min/+};*Kras*^{LSL-G12D/+};*Vil1*^{Cre};*Lgr5*^{DTR/eGFP} (AKVL) animals (Fig. 1a) carry two of the most frequently mutated genes found in human colorectal cancer and, in addition, express a diphtheria toxin receptor (DTR) fused to an enhanced green fluorescent protein (eGFP) under the endogenous regulatory region of *Lgr5*. As a result, $Lgr5^+$ cells can be visualized and ablated selectively after administration of diphtheria toxin (DT). Although these animals form polyps that contain $Lgr5^+$ cells, the animals are not suitable to study the contribution of these cells to tumour growth because long-term DT treatment results in toxicity linked to expression of *Lgr5* in other tissues, including the liver^{15,16}. Therefore, we established primary AKVL organoid tumour cultures amenable for transplantation into recipient animals that express wild-type (WT) *Lgr5* (*Lgr5*^{WT}). As previously described, removal of R-spondin and epidermal growth factor (EGF)

from the intestinal crypt culture medium allows the selective *in vitro* expansion of cystic *Apc*^{min} and *Kras*^{G12D} mutant cells over time^{17–19} (Fig. 1b). To generate organoid models that recapitulate the colorectal cancer progression paradigm², we sequentially introduced *Trp53* (AKVPL) and *Smad4* (AKVPSL) gene mutations using CRISPR–Cas9 genome editing (Fig. 1c, d and Methods). The resulting organoids were sequenced to validate the presence of frameshift-inducing insertions and deletions (indels) at the targeted loci (Extended Data Fig. 1a, b), and to confirm the absence of any alterations at predicted off-target sites for the single-guide RNAs (sgRNAs) that were used (Extended Data Fig. 1c, d and Supplementary Table 1). In addition, we functionally validated *Trp53* and *Smad4* pathway inactivation by analysing the expression levels of canonical target genes (Extended Data Fig. 1e, f). Finally, we determined the level of chromosomal instability, a hallmark of colorectal cancer progression, and observed moderate aneuploidy in both the AKVL and AKVPL mutants, whereas extensive aneuploidy was evident in AKVPSL organoids (Fig. 1e, f).

To test the effect of the increasing number of driver mutations and chromosomal instability on tumour growth *in vivo*, we subcutaneously transplanted organoids from each genotype in mice and followed their progression longitudinally. While AKVL- and AKVPL-derived tumours exhibited indolent and moderate growth, respectively, AKVPSL-derived tumours grew exponentially (Fig. 1g). In line with these distinct growth properties, histopathological evaluation showed a low proliferative index for AKVL tumours, and progressively increasing proliferation in AKVPL and AKVPSL grafts (Fig. 1h). To compare the tumorigenic capacity of AKVPL and AKVPSL organoids directly, we transplanted limiting dilutions of bulk tumour cells from each line *in vivo*. The tumour-initiating capacity, an attribute closely associated with CSC potential²⁰, was significantly higher in AKVPSL compared to AKVPL (Extended Data Fig. 2a). Therefore, it seems that the growth characteristics of our engineered mouse organoid allografts mimic the gradual disease progression in patients as they acquire both these specific mutations² and chromosomal instability^{21,22}. These data are

¹Molecular Oncology, Genentech, 1 DNA Way, South San Francisco, California 94080, USA. ²Cancer Immunology, Genentech, 1 DNA Way, South San Francisco, California 94080, USA. ³Research Pathology, Genentech, 1 DNA Way, South San Francisco, California 94080, USA. ⁴Molecular Biology, Genentech, 1 DNA Way, South San Francisco, California 94080, USA. ⁵Bioinformatics and Computational Biology, Genentech, 1 DNA Way, South San Francisco, California 94080, USA.

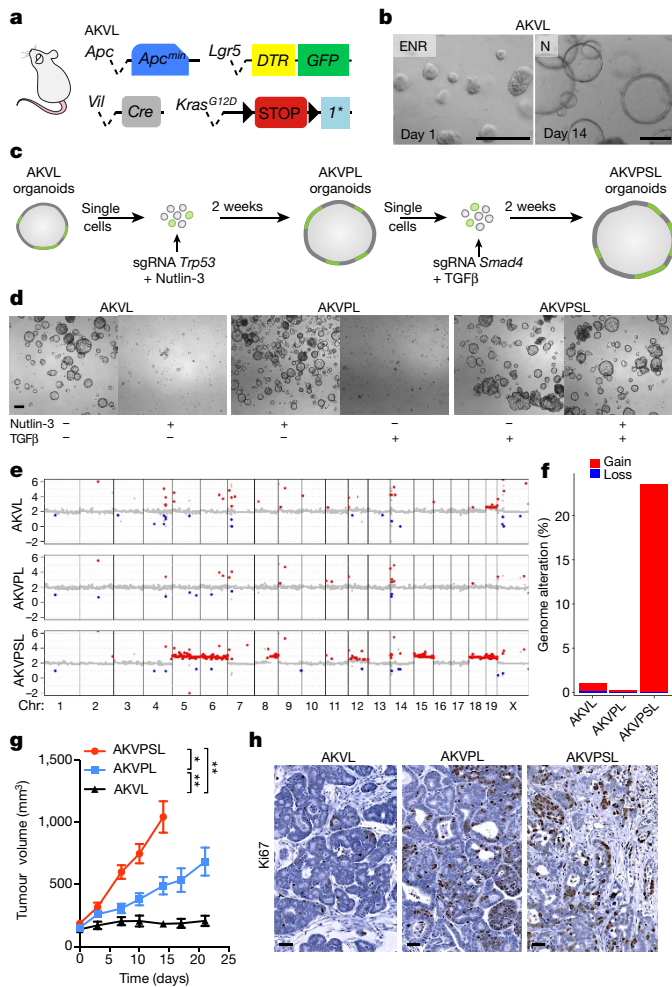


Figure 1 | Engineering, characterization and engraftment of mouse-derived intestinal tumour organoids. **a**, Genotype used to study the role of *Lgr5*⁺ cells in a mouse model of colorectal cancer. AKVL, A: *Apc*^{min/+}; K: *Kras*^{LSL-G12D/+}; V: *Vill*^{Cre}; L: *Lgr5*^{DTR/eGFP}. **b**, AKVL organoids were established in ENR (E: EGF; N: noggin; R: R-spondin) media before *Apc*^{min}/*Kras*^{G12D} mutant clones were selected in noggin-only media. **c**, CRISPR-Cas9 strategy used to generate mutant organoid lines. P: *Trp53*; S: *Smad4*; green depicts *Lgr5*-GFP⁺ cells among single cells and within organoids. **d**, Culture conditions for selection of mutant organoids. **e**, Copy-number alterations in each organoid line (red, gain; blue, loss; Chr: chromosome). **f**, Per cent genome alteration for each organoid line. **g**, Growth rate of subcutaneous organoid allografts. Mean tumour volumes ± s.e.m. are shown for AKVPSL (*n* = 8), AKVPL (*n* = 5) and AKVL (*n* = 4). **h**, Representative images of Ki67 staining of subcutaneous tumours (*n* = 4 per organoid line). Scale bars, 125 μm (**b**), 500 μm (**d**), 20 μm (**h**). **P* < 0.05, ***P* < 0.01; *n* represents the number of independent animals.

also consistent with previous reports demonstrating that the number of driver mutations in human-derived intestinal organoids is proportional to their tumorigenic capacity and the extent of chromosomal instability^{17,18}.

Lgr5 marks tumour-initiating cells

We next evaluated the effect of genotype on phenotypic attributes of CSCs. Immunostaining and fluorescence-activated cell sorting (FACS) of tumours collected five weeks after engraftment revealed an increase in the fraction of *Lgr5*-GFP⁺ cells in AKVPSL compared to AKVPL grafts (Extended Data Fig. 2b, c), suggesting that the increased tumorigenic potential correlates with an increased CSC content. This appears to be at least in part a cell-intrinsic property, as this correlation was also observed in cultured organoids that lack

stroma (Extended Data Fig. 2d, e). Previous analysis of *Lgr5*⁺ cells in mouse models of intestinal tumorigenesis had mainly been restricted to early-adenomatous lesions⁸, which are typically benign tumours and probably follow the growth dynamics of AKVL allografts. To define the molecular properties of these cells in more aggressive tumours, we transcriptionally profiled FACS-isolated *Lgr5*-GFP⁺ cells from AKVPL and AKVPSL tumours (Extended Data Fig. 3a). These cells were enriched for genes previously shown to be expressed by normal intestinal stem cells²³ and also showed increased expression of canonical Wnt target genes²⁴, when compared to *Lgr5*-GFP⁻ tumour cells (Extended Data Fig. 3b, c). To further define the tumorigenic potential of *Lgr5*-GFP⁺ cells within each genotype, we performed limiting-dilution transplants of FACS-sorted tumour cells. Tumour-engraftment analysis revealed that tumour-initiating capacity was enriched in the *Lgr5*-GFP⁺ tumour-cell fractions (Extended Data Fig. 3d, e). These grafts contained both *Lgr5*-GFP⁺ and *Lgr5*-GFP⁻ cells, confirming their ability to self-renew and to give rise to more differentiated progeny. Taken together, our results demonstrate that *Lgr5*⁺ cells exhibit important biological properties closely associated with cancer stemness. Notably, tumours that eventually grew after transplantation of *Lgr5*⁻ cells also contained a sub-population of *Lgr5*⁺ cells, which is consistent with the concept of stemness being a dynamic rather than a fixed trait in colon cancer^{9,25} (Extended Data Fig. 3f).

Lgr5⁺ CSC depletion does not lead to tumour regression

Next, we took advantage of the *Lgr5*^{DTR/eGFP} allele to study the requirement of *Lgr5*⁺ CSCs during tumour growth. AKVPL organoids that had been transplanted into immune-compromised *Lgr5*^{WT} animals allow tumour-specific *Lgr5*⁺ cell ablation for extended periods of time (Fig. 2a, b). Administration of DT resulted in tumour stasis for as long as DT treatment was continued (Fig. 2b, c). Notably, treatment discontinuation quickly led to re-initiation of tumour growth (Fig. 2c), indicating that sustained *Lgr5*⁺ cell depletion is required to prevent tumour progression. The rapid regrowth of tumours even after a prolonged (three-week) period of DT treatment directly challenges the idea that selectively killing colon CSCs may lead to colorectal tumour regression²⁶.

The tumour stasis observed during continuous depletion of CSCs prompted us to further explore the dynamics of *Lgr5*⁺ cell ablation. We performed immunostaining and FACS analysis of tumour tissues at various time points during treatment (Fig. 2d–h). A single dose of DT resulted in a complete loss of all *Lgr5*-GFP⁺ cells (Fig. 2d, e and Extended Data Fig. 4a, b), and these cells remained absent from the tumour mass upon prolonged DT treatment (Fig. 2f). However, tumours that were collected one week after DT treatment had regained their full complement of *Lgr5*-GFP⁺ cells when compared to vehicle-treated controls (Fig. 2g, h). These newly recovered *Lgr5*-GFP⁺ cells functionally contributed to tumour regrowth, as DT re-dosing affected tumour growth again (Extended Data Fig. 4c, d). Notably, the dynamics of tumour growth in response to DT-mediated depletion of *Lgr5*-GFP⁺ cells was highly similar between genotypes (Extended Data Fig. 4e, f) and was fully recapitulated in organoid cultures (Fig. 2i), indicating that *Lgr5*⁺ cell recovery can take place in the absence of tumour stroma.

To gain better insights into the molecular mechanisms that contribute to tumour regrowth, we performed a time-course analysis of transcriptional changes that occurred in tumour cells after a single dose of DT *in vivo*. Differential expression analysis showed that the molecular profiles of DT-treated tumours were highly divergent from vehicle-treated tumours 24h after DT treatment, but became concordant again following a 96-h recovery (Extended Data Fig. 5a, b and Supplementary Table 2), consistent with the idea that the *Lgr5*⁺ cell state is reversible. Gene ontology analysis indicated that the transcriptome of DT-treated tumours at 24h after DT treatment displayed an interferon-α response and activation of *Myc* signalling (Fig. 2j

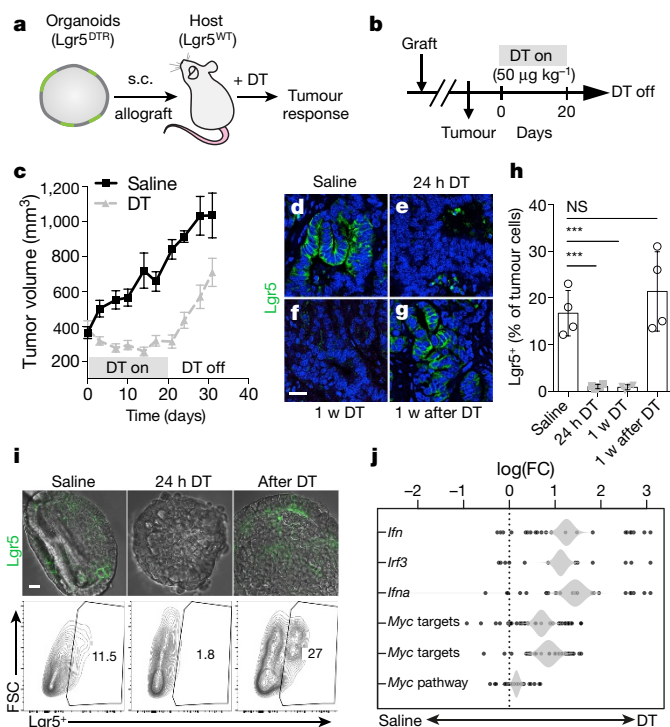


Figure 2 | Selective depletion of $Lgr5^+$ cells reveals a dependency on CSCs for subcutaneous tumour growth. **a**, Strategy for tumour-specific $Lgr5$ -lineage depletion. s.c., subcutaneous. **b**, Diphtheria toxin (DT) dosing schedule (applied every other day during the 'DT on' phase). **c**, Growth rate of subcutaneous AKVPL tumours in response to treatment. Mean tumour volumes \pm s.e.m. are shown for saline ($n = 11$) and DT ($n = 10$). **d–g**, Representative images of $Lgr5$ -GFP $^+$ staining of subcutaneous AKVPL tumours collected either during or one week after DT treatment ($n = 4$ per condition). **h**, Per cent $Lgr5$ -GFP $^+$ cells in subcutaneous AKVPL tumours collected at indicated time points (mean \pm s.d., $n = 4$ tumours per condition). **i**, Immunostaining (top) and FACS analysis (bottom) of $Lgr5$ -GFP $^+$ cells in cultured AKVPL organoids either during or 4 days after DT treatment. Representative images and FACS plots are shown from two independent experiments. **j**, Quantitative set analysis for gene expression (QuSAGE) of indicated gene signatures in DT- versus saline-treated subcutaneous AKVPL tumours 24 h after treatment. Scale bars, 20 μ m (**d–g**), 10 μ m (**i**). *** $P < 0.001$; NS, not significant; n represents the number of independent animals.

and Supplementary Table 3). While the former may reflect the response of tumour cells to tissue injury and cell death, the latter is reminiscent of normal intestinal tissue regeneration after damage²⁷. We also found an overrepresentation of genes involved in cell-cycle progression (Extended Data Fig. 5c). Accordingly, proliferation was readily detected in tumours during the course of DT treatment (Extended Data Fig. 5d). This observation is in line with the rapid tumour regrowth observed after cessation of DT treatment, and is also consistent with a recent study where $Lgr5^+$ cells were pharmacologically depleted using an antibody drug conjugate⁶. Furthermore, the molecular profile of $Lgr5^-$ cells did not reveal an enrichment of one particular intestinal cell lineage after DT treatment (Extended Data Fig. 6a and Supplementary Table 4). Therefore, the reappearance of $Lgr5$ -GFP $^+$ cells after DT treatment is reminiscent of the stem-cell plasticity observed in the normal intestine upon $Lgr5^+$ cell depletion or injury^{15,28}, where various types of $Lgr5^-$ cells can revert back to a $Lgr5^+$ stem-cell state^{15,29,30}. Notably, we did not observe an obvious increase in differentiation upon $Lgr5^+$ cell ablation (Extended Data Fig. 6b). This is in contrast to the situation we have previously described for RSPO3-fusion-positive colorectal cancer³¹. In this tumour subset, interference with RSPO3 signalling led to a rapid loss of CSC function, which resulted in reduced tumorigenicity with a concomitant increase in

differentiation. Thus, depleting CSCs from the tumour cell population is not the same as blocking oncogenic signals that are essential to acquire and/or maintain cancer stemness. Collectively, our data show that tumours are maintained by proliferating $Lgr5^-$ cells in the absence of $Lgr5^+$ CSCs. However, these $Lgr5^-$ cells are not functionally equivalent to $Lgr5^+$ CSCs, as they cannot fuel tumour growth as efficiently at least in the context of the AKVPL and AKVPSL genotypes analysed here.

$Lgr5^+$ cells are essential for metastasis

Although hypothesized by many, evidence supporting the causal relationship between CSCs and metastasis is still lacking. Unfortunately, our subcutaneously transplanted tumours never led to the development of metastasis. To circumvent this issue, we developed an orthotopic model by injecting organoids directly into the colonic mucosa (Fig. 3a), which yielded tumours that grew at a single location within the colon (Fig. 3b). We found that mice with an AKVPSL tumour in the colon had reduced survival rates compared to animals with an AKVPL graft at the same orthotopic site (Fig. 3c), in line with clinical evidence suggesting that the level of chromosomal instability is an important predictor of patient overall survival²¹. We next transduced organoids with a lentivirus co-expressing red fluorescent protein (RFP) and luciferase (Luc) to facilitate FACS identification of all tumour cells and to monitor tumour growth by bioluminescence imaging (Fig. 3d). AKVPL tumours only grew at the site of injection and showed no evidence of tumour cell dissemination to other organs, when they were evaluated six weeks after tumour implantation in the colon (Fig. 3d). By contrast, AKVPSL tumours disseminated as early as three weeks after injection, primarily to the liver (Fig. 3d–f). Furthermore, both the fraction of AKVPSL-injected animals that displayed disseminated disease as well as the extent of metastatic burden per animal increased over time (Fig. 3e, f). Notably, FACS analysis revealed enrichment of $Lgr5$ -GFP $^+$ cells in micro-metastasis (5 weeks after injection) compared to both primary tumours and macro-metastasis (6 weeks after injection) (Fig. 3g), suggesting that dissemination and/or colonization of distant sites may originate from $Lgr5^+$ CSCs.

To further investigate the importance of $Lgr5^+$ CSCs during the metastatic process, we initiated DT treatment two weeks after implantation of AKVPSL organoids in the colonic mucosa (Fig. 3h), well before metastasis can be detected by either bioluminescence imaging or histological evaluation of the entire liver (Fig. 3f). After three weeks of DT treatment, we analysed liver tissues from animals with equivalent tumour burden at the orthotopic site (Extended Data Fig. 7a). Notably, even though DT treatment did not impair the ability of tumour cells to invade the submucosa (Extended Data Fig. 7b), both bioluminescence imaging and histopathological analysis showed a substantial decrease in liver metastatic burden (Fig. 3i, j and Extended Data Fig. 7c, d). In addition, FACS analysis of enzymatically dissociated livers demonstrated a marked decrease in the absolute number of RFP $^+$ tumour cells following treatment with DT (Fig. 3k), confirming that CSCs play a noteworthy role in the initiation of metastasis.

Lastly, we evaluated the requirement of $Lgr5^+$ CSCs for the maintenance of established liver metastasis, as patients with metastatic disease currently have a poor prognosis and represent an important unmet medical need. Injection of organoids directly into the portal vein led to the formation of liver metastasis in the absence of a primary tumour (Fig. 4a and Extended Data Fig. 8a, b). Remarkably, DT treatment profoundly reduced tumour burden in the liver (Extended Data Fig. 8c) with little evidence of metastasis up to two weeks after the last dose of DT (Fig. 4b–g and Extended Data Fig. 8d–f). Livers from control mice displayed extensive metastatic disease, whereas residual disease in DT-treated animals was limited to occasional metastatic foci (Fig. 4h, i). Collectively these data are consistent with a notable role for $Lgr5^+$ CSCs in supporting liver metastasis and highlight that their functional contribution during colorectal cancer maintenance is influenced by tissue location and tumour microenvironment.

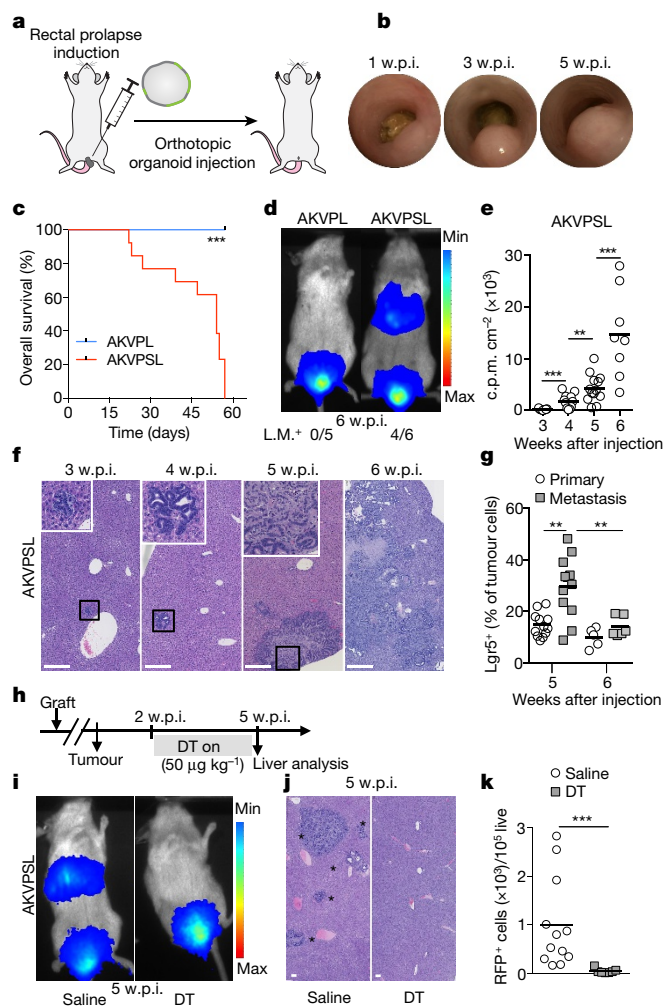


Figure 3 | $Lgr5^+$ CSCs are required for the formation of liver metastasis.

a, Schematic for orthotopic implantation of organoids. **b**, Growth of an orthotopic AKVPL tumour monitored by endoscopy at the indicated time points. **c**, Kaplan–Meier survival curve of mice with orthotopic AKVPL ($n = 9$) or AKVPSL ($n = 13$) tumours ($***P < 0.001$ by log-rank test). **d**, Representative bioluminescent images of mice with an orthotopic AKVPL ($n = 5$) or AKVPSL ($n = 6$) tumour (L.M.⁺, positive for liver metastasis). **e**, Quantification of the bioluminescence signal in the liver of mice with an orthotopic AKVPSL tumour at 3 ($n = 8$), 4 ($n = 10$), 5 ($n = 12$) and 6 ($n = 7$) weeks after implantation. c.p.m., counts per minute. **f**, Representative images of liver sections stained with haematoxylin and eosin from animals with orthotopic AKVPSL tumours collected at indicated time points ($n = 6$ per time point). Boxed areas show tumour cells at a higher magnification. **g**, Per cent $Lgr5$ -GFP⁺ cells in primary tumours and corresponding liver metastasis determined by FACS at 5 ($n = 11$) and 6 ($n = 6$) weeks after implantation. **h**, DT dosing schedule for $Lgr5$ -lineage ablation in orthotopic tumours. **i**, Representative bioluminescent images of mice with an orthotopic AKVPSL tumour after the indicated time and treatment ($n = 12$ for saline and $n = 8$ for DT). **j**, Representative images of liver sections stained with haematoxylin and eosin from saline- and DT-treated animals with an orthotopic AKVPSL tumour ($n \geq 6$ per treatment group; asterisks indicate metastatic foci). **k**, Number of RFP⁺ tumour cells in enzymatically dissociated livers of mice with an orthotopic AKVPSL tumour after the indicated treatment (FACS data are represented as means (lines) and individual tumours (circles or squares); $n \geq 8$ per treatment group). w.p.i., weeks post-injection. Scale bars, 500 μm (f, j). $**P < 0.01$, $***P < 0.001$; n represents the number of independent animals.

Discussion

Together, our data provide a comprehensive analysis of $Lgr5^+$ CSCs in colon tumorigenesis, including their role in tumour initiation, growth and metastasis. Contrary to expectations, depletion of CSCs

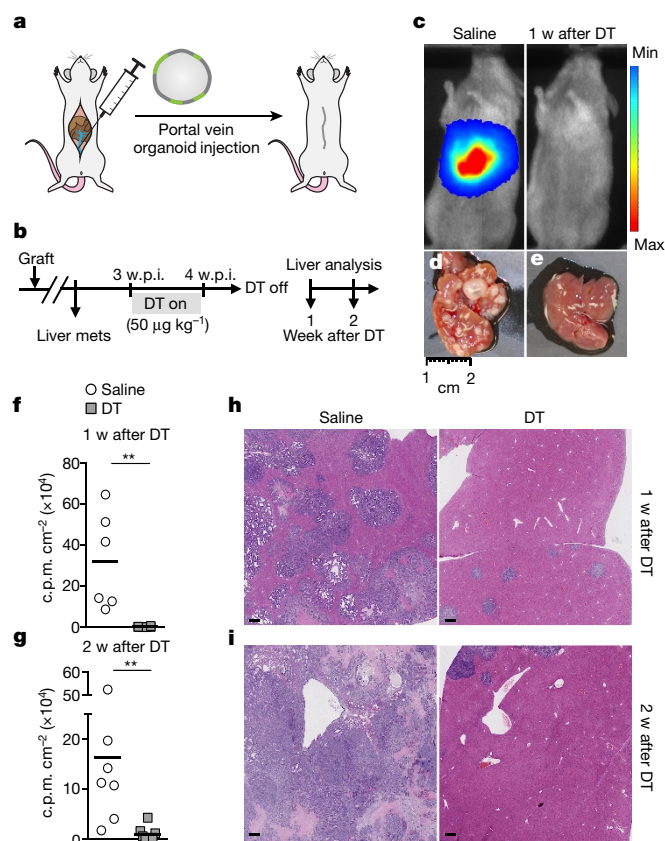


Figure 4 | $Lgr5^+$ CSCs are essential for the maintenance of colon-cancer-derived liver metastasis. **a**, Schematic for injection of portal veins with organoids to establish liver metastasis without a primary tumour.

b, DT dosing schedule of mice with liver metastasis. **c–e**, Representative bioluminescent images (**c**) and corresponding livers (**d, e**) from either saline- or DT-treated animals with liver metastasis that were collected one week after treatment ($n = 6$ per treatment group). **f, g**, Quantification of the bioluminescence signal in saline- and DT-treated animals with liver metastasis either 1 (**f**; $n = 6$ per group) or 2 (**g**; $n = 7$ per group) weeks after treatment. **h**, Representative images of liver sections stained with haematoxylin and eosin from saline- and DT-treated animals with liver metastasis ($n = 4$ per time point and treatment group). Note the extensive metastatic involvement in control livers, whereas only micro-metastases are present in livers from DT-treated animals. Scale bars, 300 μm (**h**). $**P < 0.01$; n represents the number of independent animals.

in primary tumours does neither lead to exhaustion of the proliferative transit-amplifying cell compartment nor to tumour regression. Instead, plasticity appears to enable tumour maintenance once $Lgr5^+$ cells have been ablated, although it is not able to fuel tumour growth as efficiently. Indeed, in the absence of $Lgr5^+$ CSCs, tumours are maintained by proliferative $Lgr5^-$ cancer cells, which constantly attempt to replenish the CSC pool. $Lgr5^+$ CSCs reappear upon treatment discontinuation, leading to rapid tumour regrowth. This is reminiscent of what has been observed in the normal intestine, where homeostasis is maintained by alternative cell compartments that compensate for $Lgr5^+$ cell loss³², but these are unable to drive regeneration following injury caused by irradiation or chemotherapy³³. While we surmise that CSCs are functionally relevant for primary tumour growth, our work suggests that blocking the biological cues mediating CSC plasticity will be required to provide a durable benefit⁹.

Additionally, our findings underscore a critical role for $Lgr5^+$ CSCs during the development and maintenance of colorectal-cancer-derived metastasis and imply that patients with unresectable liver metastasis potentially may benefit from targeting CSCs. While the exact mechanism by which distinct environmental cues influence tumour regrowth after CSC depletion remain to be fully established, our data suggest

that certain tissue-specific milieux may be more permissive (that is, colon) than others (that is, liver) for plasticity of epithelial tumour cells. Indeed, a similar requirement for CD36⁺ cells during dissemination, but not primary tumour growth, was recently observed in oral carcinomas³⁴. The models of orthotopic and metastatic colorectal cancer that we have developed here should permit characterization of these biological responses in greater detail.

Online Content Methods, along with any additional Extended Data display items and Source Data, are available in the online version of the paper; references unique to these sections appear only in the online paper.

Received 20 July 2016; accepted 18 February 2017.

- Siegel, R., Desantis, C. & Jemal, A. Colorectal cancer statistics, 2014. *CA Cancer J. Clin.* **64**, 104–117 (2014).
- Fearon, E. R. & Vogelstein, B. A genetic model for colorectal tumorigenesis. *Cell* **61**, 759–767 (1990).
- O'Brien, C. A., Pollett, A., Gallinger, S. & Dick, J. E. A human colon cancer cell capable of initiating tumour growth in immunodeficient mice. *Nature* **445**, 106–110 (2007).
- Ricci-Vitiani, L. *et al.* Identification and expansion of human colon-cancer-initiating cells. *Nature* **445**, 111–115 (2007).
- Barker, N. *et al.* Crypt stem cells as the cells-of-origin of intestinal cancer. *Nature* **457**, 608–611 (2009).
- Junttila, M. R. *et al.* Targeting LGR5⁺ cells with an antibody-drug conjugate for the treatment of colon cancer. *Sci. Transl. Med.* **7**, 314ra186 (2015).
- Kemper, K. *et al.* Monoclonal antibodies against LGR5 identify human colorectal cancer stem cells. *Stem Cells* **30**, 2378–2386 (2012).
- Schepers, A. G. *et al.* Lineage tracing reveals Lgr5⁺ stem cell activity in mouse intestinal adenomas. *Science* **337**, 730–735 (2012).
- Vermeulen, L., de Sousa e Melo, F., Richel, D. J. & Medema, J. P. The developing cancer stem-cell model: clinical challenges and opportunities. *Lancet Oncol.* **13**, e83–e89 (2012).
- Al-Hajj, M., Wicha, M. S., Benito-Hernandez, A., Morrison, S. J. & Clarke, M. F. Prospective identification of tumorigenic breast cancer cells. *Proc. Natl Acad. Sci. USA* **100**, 3983–3988 (2003).
- Singh, S. K. *et al.* Identification of human brain tumour initiating cells. *Nature* **432**, 396–401 (2004).
- Chen, J. *et al.* A restricted cell population propagates glioblastoma growth after chemotherapy. *Nature* **488**, 522–526 (2012).
- Boumahdi, S. *et al.* SOX2 controls tumour initiation and cancer stem-cell functions in squamous-cell carcinoma. *Nature* **511**, 246–250 (2014).
- Enquist, I. B. *et al.* Lymph node-independent liver metastasis in a model of metastatic colorectal cancer. *Nat. Commun.* **5**, 3530 (2014).
- Tian, H. *et al.* A reserve stem cell population in small intestine renders Lgr5-positive cells dispensable. *Nature* **478**, 255–259 (2011).
- Huch, M. *et al.* *In vitro* expansion of single Lgr5⁺ liver stem cells induced by Wnt-driven regeneration. *Nature* **494**, 247–250 (2013).
- Drost, J. *et al.* Sequential cancer mutations in cultured human intestinal stem cells. *Nature* **521**, 43–47 (2015).
- Matano, M. *et al.* Modeling colorectal cancer using CRISPR-Cas9-mediated engineering of human intestinal organoids. *Nat. Med.* **21**, 256–262 (2015).
- Schwank, G. *et al.* Functional repair of CFTR by CRISPR/Cas9 in intestinal stem cell organoids of cystic fibrosis patients. *Cell Stem Cell* **13**, 653–658 (2013).
- Clarke, M. F. *et al.* Cancer stem cells—perspectives on current status and future directions: AACR workshop on cancer stem cells. *Cancer Res.* **66**, 9339–9344 (2006).
- Sheffer, M. *et al.* Association of survival and disease progression with chromosomal instability: a genomic exploration of colorectal cancer. *Proc. Natl Acad. Sci. USA* **106**, 7131–7136 (2009).
- Walther, A., Houlston, R. & Tomlinson, I. Association between chromosomal instability and prognosis in colorectal cancer: a meta-analysis. *Gut* **57**, 941–950 (2008).
- Muñoz, J. *et al.* The Lgr5 intestinal stem cell signature: robust expression of proposed quiescent '+4' cell markers. *EMBO J.* **31**, 3079–3091 (2012).
- Kim, T. H. *et al.* Single-cell transcript profiles reveal multilineage priming in early progenitors derived from Lgr5⁺ intestinal stem cells. *Cell Reports* **16**, 2053–2060 (2016).
- Vermeulen, L. *et al.* Wnt activity defines colon cancer stem cells and is regulated by the microenvironment. *Nat. Cell Biol.* **12**, 468–476 (2010).
- Kaiser, J. The cancer stem cell gamble. *Science* **347**, 226–229 (2015).
- Ashton, G. H. *et al.* Focal adhesion kinase is required for intestinal regeneration and tumorigenesis downstream of Wnt/c-Myc signaling. *Dev. Cell* **19**, 259–269 (2010).
- Ritsma, L. *et al.* Intestinal crypt homeostasis revealed at single-stem-cell level by *in vivo* live imaging. *Nature* **507**, 362–365 (2014).
- Asfaha, S. *et al.* Krt19⁺/Lgr5⁺ cells are radioresistant cancer-initiating stem cells in the colon and intestine. *Cell Stem Cell* **16**, 627–638 (2015).
- Tetteh, P. W. *et al.* Replacement of lost Lgr5-positive stem cells through plasticity of their enterocyte-lineage daughters. *Cell Stem Cell* **18**, 203–213 (2016).
- Storm, E. E. *et al.* Targeting PTPRK-RSPO3 colon tumours promotes differentiation and loss of stem-cell function. *Nature* **529**, 97–100 (2016).
- Beumer, J. & Clevers, H. Regulation and plasticity of intestinal stem cells during homeostasis and regeneration. *Development* **143**, 3639–3649 (2016).
- Metcalfe, C., Kljavin, N. M., Ybarra, R. & de Sauvage, F. J. Lgr5⁺ stem cells are indispensable for radiation-induced intestinal regeneration. *Cell Stem Cell* **14**, 149–159 (2014).
- Pascual, G. *et al.* Targeting metastasis-initiating cells through the fatty acid receptor CD36. *Nature* **541**, 41–45 (2017).

Supplementary Information is available in the online version of the paper.

Acknowledgements We thank M. Junttila and K. Leong for generation of the AKVL mouse model, A. Bruce for help designing schematic figures, J. Jian for tissue processing, J. Stinson and the NGS laboratory for RNA-sequencing, J. Paw, C. Poon, T. Ho and J. Borneo for flow cytometry support, members of Laboratory Animal Resources for animal care and de Sauvage laboratory members for comments on the manuscript.

Author Contributions F.d.S.M. and F.J.d.S. conceptualized the project and designed experiments. F.d.S.M. engineered and characterized all mutant organoid lines, produced concentrated lentivirus, optimized the orthotopic injection methodology and conducted bioluminescent imaging. F.d.S.M., A.V.K. and N.K. performed subcutaneous transplants, endoscopic imaging, DT treatment, tumour measurements and collected tissues. F.d.S.M. and A.V.K. conducted flow cytometry experiments. J.M.H. performed portal vein injections. G.J.P.D. modified pLKO-SHC201, cloned sgRNAs and designed pGEIL-tRFP. F.d.S.M., J.D.H., J.H., J.E.A. and E.E.S. either acquired or evaluated immunohistochemistry and/or immunofluorescence data. H.K. performed histopathological evaluation of tumour and liver tissues. Z.M. contributed next-generation sequencing data. R.P. provided bioinformatics support. F.d.S.M., G.J.P.D. and F.J.d.S. wrote the manuscript.

Author Information Reprints and permissions information is available at www.nature.com/reprints. The authors declare competing financial interests: details are available in the online version of the paper. Readers are welcome to comment on the online version of the paper. Publisher's note: Springer Nature remains neutral with regard to jurisdictional claims in published maps and institutional affiliations. Correspondence and requests for materials should be addressed to F.J.d.S. (desauvage.fred@gene.com).

Reviewer Information Nature thanks F. Greten, R. Shivdasani and the anonymous reviewer(s) for their contribution to the peer review of this work.

METHODS

Animal studies. All studies involving animals were approved by Genentech's Institutional Animal Care and Use Committee and adhere to the NRC Guidelines for the Care and Use of Laboratory Animals. Female NOD.Cg-Prkdc^{scid}Il2rg^{tm1Wjl}/SzJ (NSG) mice were purchased from the Jackson Laboratory (8–12 weeks old; stock 005557). *Apc*^{min/+} (multiple intestinal neoplasia (min)); *Kras*^{LSL-G12D/+} (*loxP*-Stop-*loxP* *Kras*^{G12D/+}); *Vill*^{Cre} (AKV) mice were described previously¹⁴ and were crossed with *Lgr5*^{DTR/eGFP} mice¹⁵ to generate AKVL animals.

Subcutaneous transplantation. Organoids were collected from Matrigel plugs using Cell Recovery Solution (Corning) and mechanically dissociated to generate small clusters of cells. Approximately 10⁵ cells were resuspended in organoid basal media, admixed with 50% Matrigel (Corning) to a final volume of 200 μ l, and injected subcutaneously in the left flank of NSG mice. Tumour dimensions were measured using calipers and tumour volume was calculated as 0.523 \times length \times width \times width. Animals were humanely euthanized according to the following criteria: clinical signs of persistent distress or pain, significant body-weight loss (>20%), tumour size exceeding 2,500 mm³, or when tumours ulcerated. Maximum tumour size permitted by the Institutional Animal Care and Use Committee (IACUC) is 3,000 mm³ and in none of the experiments was this limit exceeded.

Tumour dissociation and limiting dilution. Tumours were collected and dissociated enzymatically for 30 min with a mixture of collagenase (1.5 mg ml⁻¹; Roche) and hyaluronidase (20 μ g ml⁻¹; Sigma-Aldrich) at 37 °C. The cells were then filtered (70- μ m pore size), washed and debris was removed by either lympholyte centrifugation (M; Cedarlane) or ACK lysis. The cell suspensions were stained with the following antibodies for flow cytometry analysis: anti-EpCAM (1:1,000, APC-conjugated, Clone G8.8, Biolegends), anti-CD45 (1:1,000, APC-Cy7-conjugated, Clone 30-F11, Biolegends). Dead cells were excluded with Sytox blue (1:1,000, Invitrogen). Gating for Lin⁻, EpCAM⁺ singlet, live cells was used to determine the percentage of *Lgr5*⁺ cells. Normal colonic cells from an *Lgr5*^{WT} host were used as control, and GFP⁺ analysis gates were established so that zero GFP⁺ events were detectable in *Lgr5*^{WT} tissue specimens.

For limiting dilution analysis 100, 500 and 2,500 cells from either the 10% lowest or the 10% highest *Lgr5*-GFP intensities were deposited by FACS in a 96-well plate containing Organoid basal medium, admixed with Matrigel (50%), and injected subcutaneously as described above. Clonal frequency and statistical significance were evaluated with the Extreme Limiting Dilution Analysis (ELDA) limdil function (<http://bioinf.wehi.edu.au/software/elda/index.html>). Similarly, *in vitro* clonogenicity was evaluated by limiting dilution deposition of FACS-sorted, live, bulk tumour cells at 1, 2, 4, 6, 8, 12 and 16 cells per well in a flat-bottom 96-well plate precoated with Matrigel.

Orthotopic injection of organoids. The lumen implantation procedure has previously been described¹⁴. Briefly, mice were anaesthetized by isoflurane inhalation and injected intraperitoneally (i.p.) with buprenorphine at 0.05–0.1 mg kg⁻¹. Animals were then placed in a supine position, and the extremities secured to a gauze-covered platform with tape. A blunt-ended haemostat (Micro-Mosquito, 13010-12, Fine Science Tools) was inserted approximately 1 cm into the anus. The haemostat was angled towards the mucosa and opened slightly so that a single mucosal fold could be clasped by closing the haemostat to the first notch. The haemostat was retracted from the anus, exposing the clasped exteriorized mucosa. A 10- μ l cell suspension of organoids admixed with 50% Matrigel (Corning) was directly injected into the colonic mucosae. After rehydrating the mucosa with phosphate-buffered saline (PBS), the haemostat was released and a blunt gavage needle was used to re-insert the exteriorized colon thereby reversing the rectal prolapse.

Portal-vein injection of organoids. Portal-venous tumour cell injections were performed using a modified experimental mouse model described elsewhere³⁵. Mice were anaesthetized by isoflurane inhalation and an abdominal incision site was shaved and prepped with betadine and alcohol. Mice were placed in a supine position, and the extremities secured on a heating pad with tape to maintain body temperature at around 36 °C. Body temperature was checked using a rectal probe. A median laparotomy extending to the xyphoid cartilage was performed and the duodenum mobilized to expose the portal vein. We injected 100 μ l of bulk AKVPSL organoids equivalent to around 50,000 cells into the portal vein of each animal. Tumour cells were slowly injected over the course of 1 min using a 33-gauge needle. After careful removal of the needle, bleeding was stopped by applying gentle pressure on the injection site using cotton-tipped swabs and haemostyptic calcium-alginate fleece (Sorbalgon, Hartmann Inc.). Subsequently, the intestine was placed back, and the muscle layer and the skin were sewn shut using 6-0 vicryl, and ethilon, respectively, in a two-layer technique.

Endoscopy. Endoscopic imaging was performed exactly as described¹⁴. Before imaging, mice were anaesthetized by isoflurane inhalation, placed in a supine position, and their colons evacuated of stool using a gavage needle. Endoscopic imaging equipment consisted of a Hopkins II 0° straight-forward 1.9-mm outer

diameter telescope encompassed by an examination and protection sheath, an Image-1 high-definition three-chip digital camera attached to a Mikata Point Setter telescope-holding system, a fibre-optic-light guide cable connected to a D Light System xenon light source, an electronic CO₂ insufflator to maintain colon insufflation during imaging, and an AIDA Connect high-definition documentation system connected to a high-definition colour monitor (Karl Storz). Endoscopic videos were reviewed using VLC Media Player (VideoLAN Team) and still images were captured from these videos.

Overall survival. Animal status was recorded up to 60 days after orthotopic implantation of tumour cells. Morbidity criteria during that period of time included: animals found dead, moribund animals that had to be euthanized owing to severe weight loss (>20%), rectal prolapse that could not be reversed and animals that showed clinical signs of persistent fatigue or distress. Survival data were analysed using the standard Kaplan–Meier analysis and survival curves were compared using a log-rank test (Prism).

Bioluminescence imaging. Mice were anaesthetized using isoflurane, injected i.p. with 200 μ l of 25 mg ml⁻¹ D-luciferin (Invitrogen, L2912) using a tuberculin syringe, and imaged on the Photon Imager (BioSpace Laboratory). During image acquisition, animals continued to receive anaesthesia from a nose-cone delivery system, while their body temperatures were maintained on a thermostatically controlled platform. Photon counts per min per cm² of observational area were calculated and compared using M3 Vision software (BioSpace Laboratory).

Diphtheria toxin and BrdU treatments. DT (Millipore, # 322326) was administered via i.p. injection at a dose of 50 μ g per kg every other day for the time indicated in each experimental setup. Proliferative cells were labelled by a single i.p. injection of BrdU (30 mg per kg, BD Bioscience) two hours before tumour collection. For *in vitro* treatment of organoids, DT was added to the culture medium at a final concentration of 100 ng ml⁻¹.

Culture of mouse intestinal AKVL organoids. AKVL mouse organoids were established from isolated crypts collected from the small intestine and maintained as previously described¹⁹. Organoids were first established in basal culture medium containing advanced DMEM/F12 medium (Invitrogen), B27 (Invitrogen), *N*-acetylcysteine (Sigma-Aldrich), noggin (Peprotech), R-spondin 3 (Genentech), and EGF (Peprotech). One week after seeding, EGF and R-spondin 3 were omitted from the basal media to select for *Kras*^{G12D} and *Apc*^{min} mutant organoids.

Genome editing. Gene-specific sgRNAs were designed to target coding regions at the 5' end of *Trp53* and *Smad4* to maximize disruption. Guides with the best off-target score based on the number and location of mismatches were cloned into pLKO-SHC201, for co-expression with Cas9. At least 3 independent gRNAs were tested per gene. Organoids were dissociated into a single-cell suspension using accutase (Sigma-Aldrich) for 5 min at 37 °C and then transfected with 1 μ g of DNA using Lipofectamine 2000 (Invitrogen). Cells were washed twice with basal media 6 h after transfection, embedded in Matrigel and cultured in basal media supplemented with 1 μ M of Y-27632 (Sigma-Aldrich). *Trp53*-mutant organoids were selected by growth in the presence of 10 μ M Nutlin-3 (Sigma-Aldrich) 48 h after transfection, whereas *Smad4*-mutant organoids were cultured in the absence of Noggin and presence of TGF- β (Peprotech, 10 ng ml⁻¹).

Lentivirus production. Viral particles were produced as previously described³⁶. In brief, HEK293T cells were plated on 15-cm dishes in high glucose DMEM with 10% heat inactivated FBS 24 h before transfection. Lentiviral supernatants were prepared by co-transfection using 6 μ g of pGEIL-tRFP (EF1 α -tRFP-IRES-Luc2), 12 μ g of the packaging vector Δ 8.9, 3 μ g of the envelope vector pVSV-G (Clontech) and the transfection reagent GeneJuice (Novagen). The culture medium was replaced 12 h after transfection and viral supernatant was collected 24 h later, filtered through a 0.45- μ m PES filter (Nalgene) and stored at 4 °C until further processing. Viral supernatants were concentrated 200-fold by ultracentrifugation at 100,000g for 1 h and 30 min. Viral pellets were resuspended in organoid basal media and stored at -80 °C.

Immunostaining. Samples were formalin-fixed and paraffin-embedded using standard procedures. For Ki67 antibody stains, rehydrated sections were pressure-cooked for 15 min in antigen unmasking buffer (DAKO), blocked in serum-free protein block (DAKO) and incubated in anti-Ki67 (1:400, Sigma-Aldrich) overnight. Sections were then incubated in HRP-conjugated anti-rabbit antibody (DAKO) and detected with DAB reaction (DAKO). For immunofluorescence stains, sections were incubated overnight with either anti-CC3 (1:400, rabbit, Cell Signaling), anti-BrdU (1:400, rat, Rockland) or anti-GFP (1:100, Cell Signaling clone D5.1, XP) antibodies. The signal was further amplified by TSA (Molecular Probes, T20932) according to the manufacturer's instructions. Anti-rabbit and anti-rat conjugated to either Alexa Fluor-488 or -555 were used as secondary antibodies (1:500; Molecular Probes). Pictures were acquired with an NIKON A1R using N3 elements software.

qPCR. RNA was isolated from samples using either the RNeasy Micro or Mini kit (74004 and 74104; Qiagen). qPCR was performed in 10- μ l reactions with

50 ng total RNA using the One-step Real-time RT-PCR mastermix (4392938; Life Technologies) according to the manufacturer's instructions. Taqman probes *Actb* (Mm01205647_g1) and *p21* (Mm04205640_g1) were from Life Technologies. qPCR reactions were run on a 7900HT Fast Real-Time PCR system (ABI) at the following thermal cycling conditions: holding step of 30 min at 48 °C followed by a holding step of 10 min at 95 °C and 40 cycles of 10 s at 95 °C and 1 min at 60 °C.

RNA-sequencing. RNA-sequencing (RNA-seq) libraries were prepared with the TruSeq RNA Sample Preparation kit (Illumina, CA). The libraries were sequenced on Illumina HiSeq 2500 sequencers to obtain on average 34 million 50-bp single-end reads per sample. RNA-seq reads were first aligned to ribosomal RNA sequences to remove ribosomal reads. The remaining reads were aligned to the mouse reference genome (NCBI Build 38) using GSNAP³⁷ version 2013-10-10, allowing a maximum of two mismatches per 50-base sequence (parameters: -M 2 -n 10 -B 2 -i 1 -N 1 -w 200000 -E 1 -pairmax-rna = 200000 -clip-overlap). Transcript annotation was based on the RefSeq database (NCBI Annotation Release 104). To quantify gene expression levels, the number of reads mapped to the exons of each RefSeq gene was calculated. Read counts were scaled by library size, quantile normalized and precision weights were calculated using the voom R package³⁸. Subsequently, differential expression analysis on the normalized count data was performed using the limma R package³⁹. In addition, gene expression was obtained in the form of normalized reads per kilobase gene model per million total reads (nRPKM) as described in ref. 40.

Whole-exome and low-coverage whole-genome sequencing. Exome capture was performed using Agilent's SureSelect Mouse 50Mb baits and processed using the SureSelect version 1.5.1 protocol. Both whole-exome sequencing (WES) and whole-genome sequencing (WGS) were performed on Illumina HiSeq 2500 sequencers to obtain 75 bp paired-end reads with an average of 32 million and 111 million fragments per sample, respectively. Reads were aligned to the mouse reference genome (NCBI Build 38) using GSNAP³⁷ version 2013-10-10, allowing a maximum of two mismatches per 75-base sequence (parameters: -M 2 -n 10 -B 2 -i 1 -pairmax-dna = 1000 -terminal-threshold = 1000 -gmap-mode = none-clip-overlap).

Genotyping. We used RNA-seq data to validate the CRISPR-Cas9 modification of the *Trp53* and *SMAD4* loci. For this purpose, reads in the targeted regions were extracted from the original RNA-seq mapping data with Samtools (version 1.2)⁴¹. Subsequently, GATK (version 3.5-0) HaplotypeCaller⁴² was used to assemble haplotypes and assign reads to them (parameters: -bamWriterType ALL_POSSIBLE_HAPLOTYPES -U ALLOW_N_CIGAR_READS). Haplotype frequencies were determined using a custom in-house script.

Identification of CRISPR off-target effects. We used WES data from organoids and matching spleen to identify potential mutations in coding regions that may have been introduced by off-target binding of the CRISPR-Cas9 complex. More specifically, we used loFreq⁴³ to call single-nucleotide variants (SNVs) and indels by comparing WES from organoids of the three genotypes to WES from the spleen. At the same time, we predicted putative off-target binding regions of the gRNAs using an in-house algorithm. The predicted regions were queried for the presence of SNVs and indels, and were visually inspected using IGV⁴⁴.

Identification of copy-number alterations. To identify chromosomal aberrations we called copy-number changes in each of the three genotypes by comparing their WGS data to the sequencing data from the spleen of the donor using Control-FREEC version 9.9 with a window size of 50 kb⁴⁵.

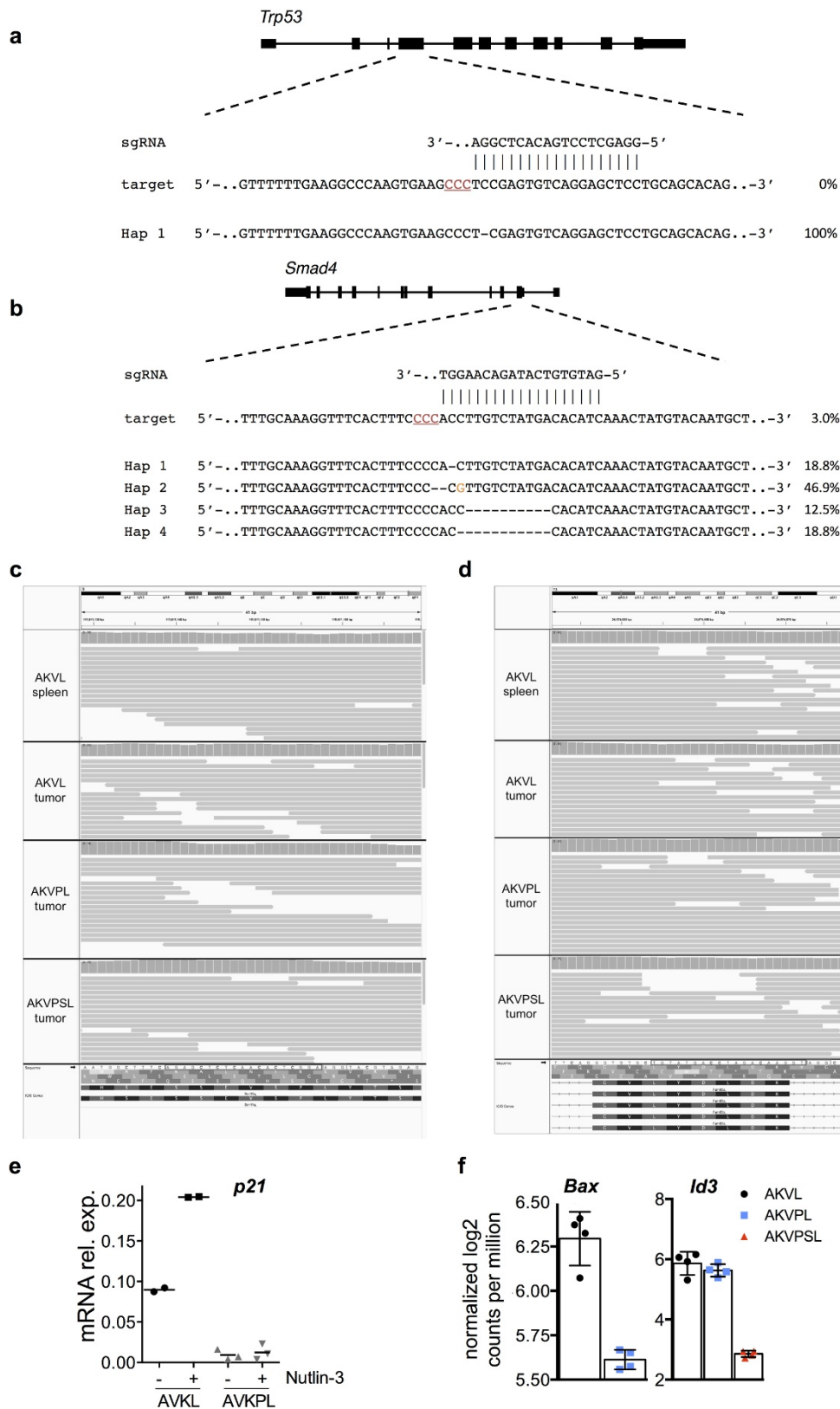
Gene-set analysis. We performed quantitative set analysis for gene expression (QuSAGE)⁴⁶ to identify relevant biological processes associated with Lgr5⁺ cell identity and depletion. For that purpose, we contrasted Lgr5⁺ with Lgr5⁻ samples or DT-treated with saline-treated samples, respectively. For each contrast we then

calculated the gene-set activity (that is, the mean difference in log expression of the individual genes that compose the set) for each of the 12,984 curated gene sets in the collection from MSigDB⁴⁷ and for selected sets from ref. 23.

Statistics. Data are represented as mean \pm s.e.m., unless stated otherwise. None of the experiments were blinded and no statistical methods were used to pre-determine sample size for *in vivo* experiments. The number of animals used for each experiment is specified in the relevant figures and legends, and was estimated based on the variability in tumour take rate and growth observed for each model. With regards to randomization, for subcutaneous transplantation, animals were distributed among treatment groups when tumours reached a mean volume of approximately 200–400 mm³. For orthotopic and portal-vein injections, mice with comparable bioluminescence signal intensity were randomized into treatment groups. Unless stated otherwise, statistical significance between two groups was determined by the Mann-Whitney *U*-test (Prism version 6.0, GraphPad Software, Inc.). All experiments were reproduced at least twice. To determine statistical significance of gene set activity, false discovery rate (FDR)-adjusted *P* values were obtained by comparing the probability distribution function of log fold changes in a given gene set (highlighted in grey) to a baseline value of zero using a one-sided test.

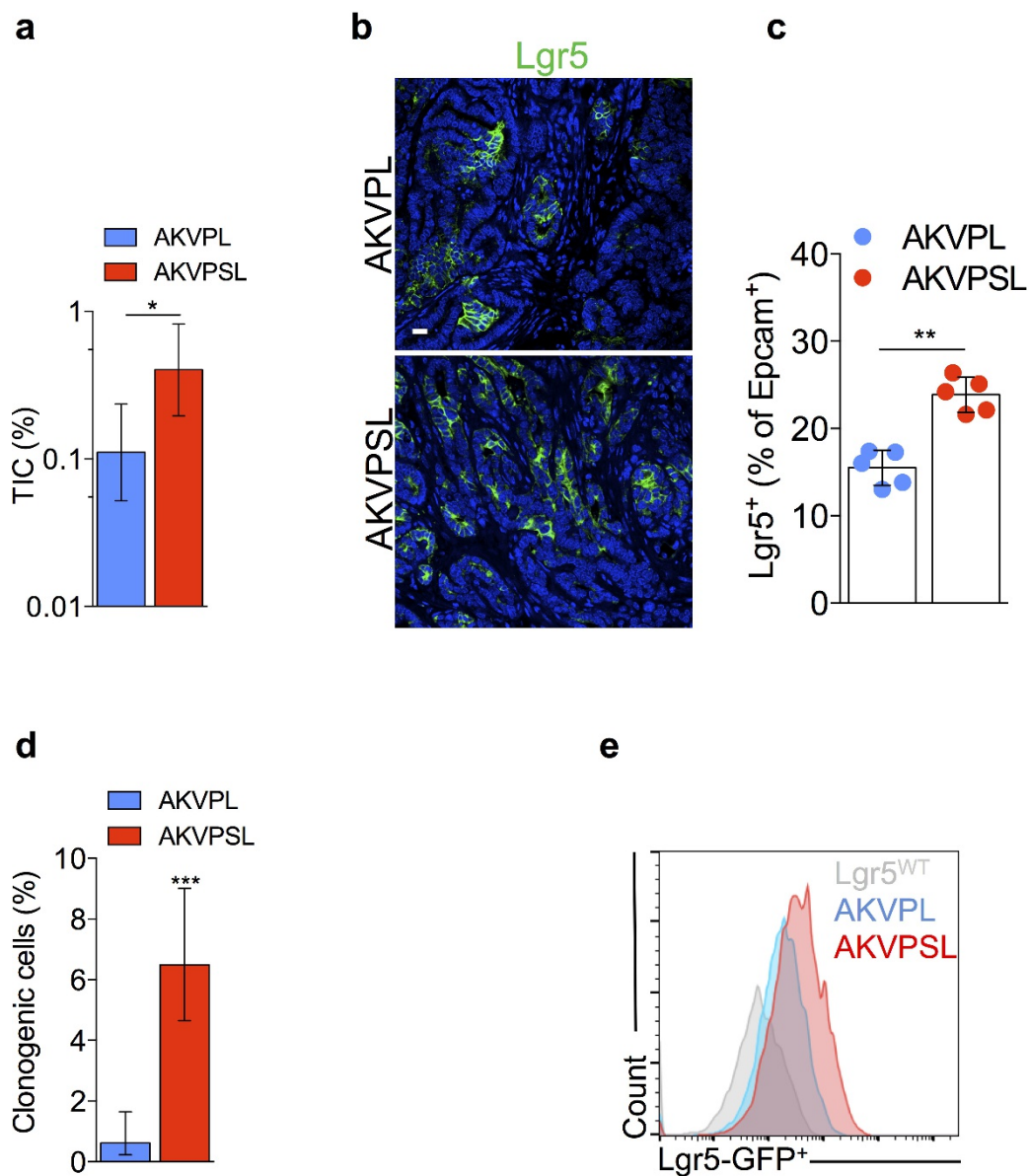
Data availability. All sequencing data from this study have been deposited in the Gene Expression Omnibus under accession number GSE92966. Source Data files underlying the graphical representation of all *in vivo* experiments can be accessed in the online version of this paper. All other data are available from the corresponding author upon reasonable request.

35. Thalheimer, A. *et al.* The intraportal injection model: a practical animal model for hepatic metastases and tumor cell dissemination in human colon cancer. *BMC Cancer* **9**, 29 (2009).
36. Sharpe, H. J. *et al.* Genomic analysis of smoothed inhibitor resistance in basal cell carcinoma. *Cancer Cell* **27**, 327–341 (2015).
37. Wu, T. D. & Nacu, S. Fast and SNP-tolerant detection of complex variants and splicing in short reads. *Bioinformatics* **26**, 873–881 (2010).
38. Law, C. W., Chen, Y., Shi, W. & Smyth, G. K. voom: precision weights unlock linear model analysis tools for RNA-seq read counts. *Genome Biol.* **15**, R29 (2014).
39. Ritchie, M. E. *et al.* limma powers differential expression analyses for RNA-sequencing and microarray studies. *Nucleic Acids Res.* **43**, e47 (2015).
40. Srinivasan, K. *et al.* Untangling the brain's neuroinflammatory and neurodegenerative transcriptional responses. *Nat. Commun.* **7**, 11295 (2016).
41. Li, H. *et al.* The sequence alignment/map format and SAMtools. *Bioinformatics* **25**, 2078–2079 (2009).
42. McKenna, A. *et al.* The genome analysis toolkit: a MapReduce framework for analyzing next-generation DNA sequencing data. *Genome Res.* **20**, 1297–1303 (2010).
43. Wilm, A. *et al.* LoFreq: a sequence-quality aware, ultra-sensitive variant caller for uncovering cell-population heterogeneity from high-throughput sequencing datasets. *Nucleic Acids Res.* **40**, 11189–11201 (2012).
44. Robinson, J. T. *et al.* Integrative genomics viewer. *Nat. Biotechnol.* **29**, 24–26 (2011).
45. Boeva, V. *et al.* Control-FREEC: a tool for assessing copy number and allelic content using next-generation sequencing data. *Bioinformatics* **28**, 423–425 (2012).
46. Yaari, G., Bolen, C. R., Thakar, J. & Kleinstein, S. H. Quantitative set analysis for gene expression: a method to quantify gene set differential expression including gene-gene correlations. *Nucleic Acids Res.* **41**, e170 (2013).
47. Liberzon, A. *et al.* Molecular signatures database (MSigDB) 3.0. *Bioinformatics* **27**, 1739–1740 (2011).
48. Hu, Y. & Smyth, G. K. ELDA: extreme limiting dilution analysis for comparing depleted and enriched populations in stem cell and other assays. *J. Immunol. Methods* **347**, 70–78 (2009).



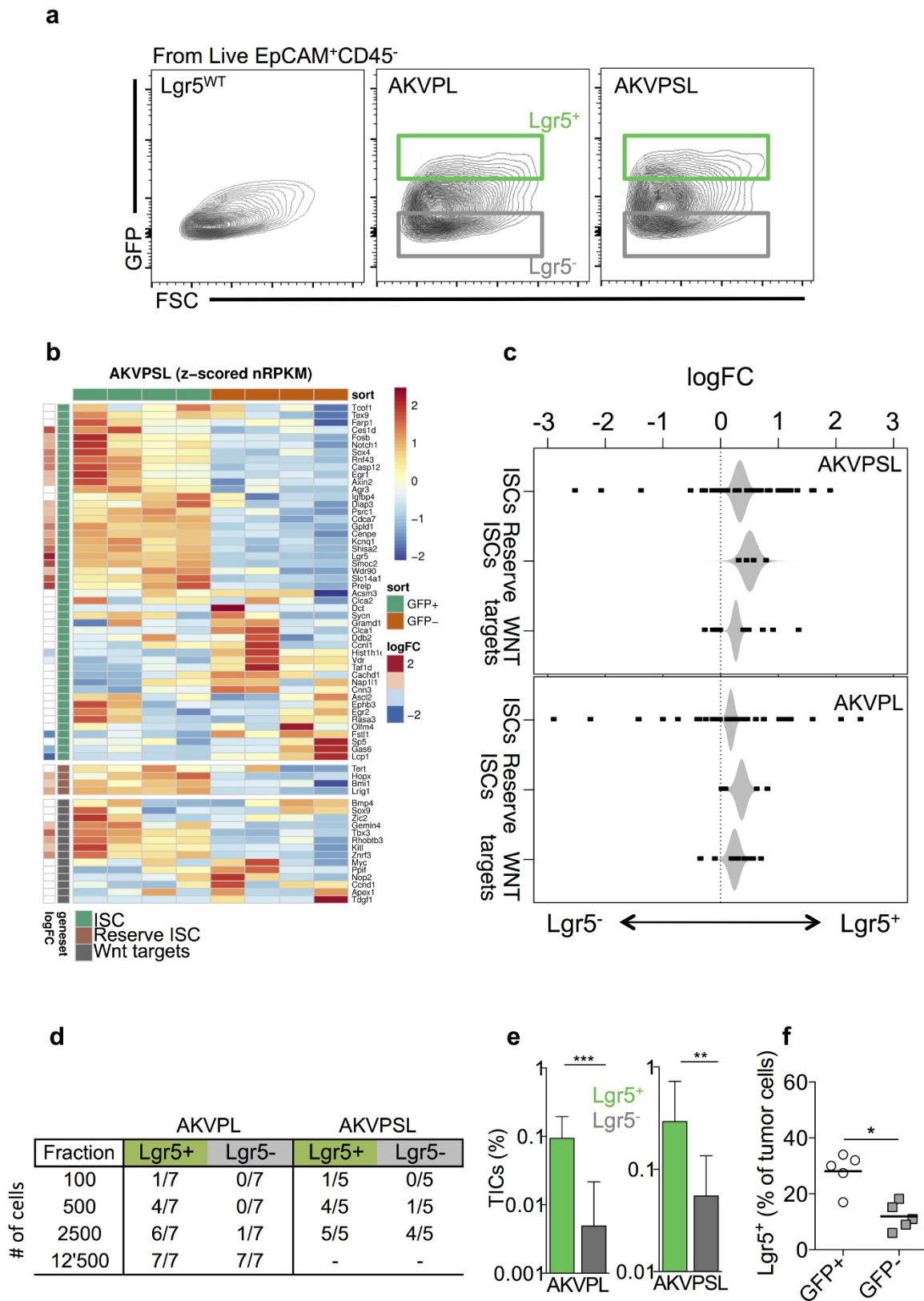
Extended Data Figure 1 | Validation of CRISPR-Cas9-mediated gene targeting. **a, b**, Gene-targeting strategy for *Trp53* (**a**) and *Smad4* (**b**). The protospacer adjacent motif (PAM) is underlined on the target sequence and the allelic fraction of each haplotype is indicated. **c, d**, Sequence alignment of exome-sequencing reads at a representative predicted off-target site for one of the sgRNAs used to mutate either *Trp53* (**c**) or *Smad4* (**d**). Of note, neither single-nucleotide variants nor copy-number changes could be detected. **e**, Relative *p21* (also known as

Cdkn1a) expression in AKVL and AKVPL organoids cultured in either the presence or absence of Nutlin-3 (qPCR data was normalized to *Actb*; $n = 2$ independent AKVL clones; $n = 3$ independent AKVPL clones generated by 2 different sgRNAs targeting *Trp53*). **f**, Relative expression of *Bax* (a canonical *Trp53*-target gene) and *Id3* (a canonical *Smad4*-target gene) in organoids with indicated genotype (RNA-seq expression analysis was quantile normalized and represented as log₂ counts per million).



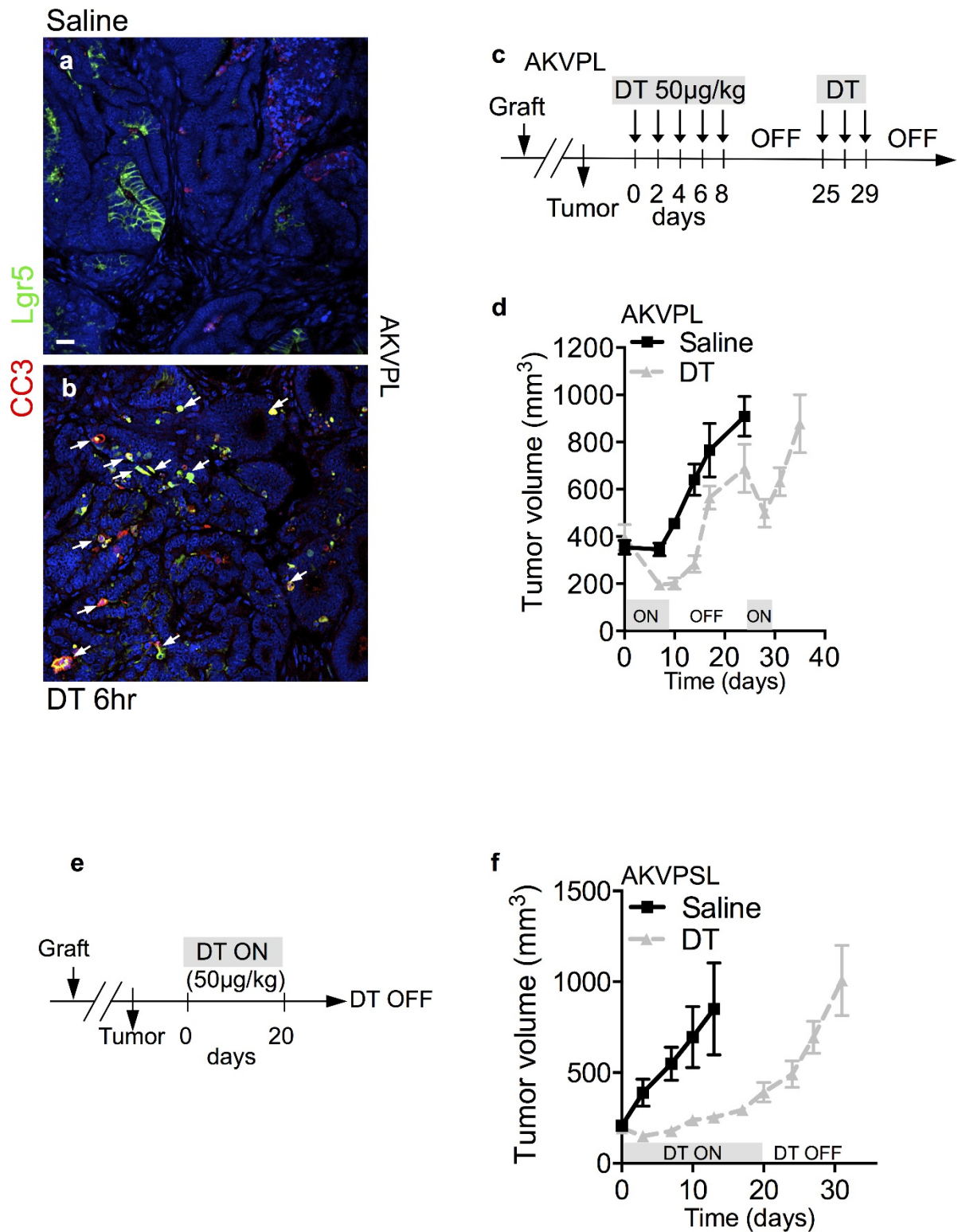
Extended Data Figure 2 | Genotype affects CSC content and tumorigenic capacity. **a**, Per cent tumour-initiating cells (TIC) in subcutaneous AKVPL and AKVPSL tumours estimated with the extreme limiting dilution analysis (ELDA⁴⁸; $n = 6$ allografts per dilution; error bars represent the 95% confidence interval). **b**, Representative images of Lgr5-GFP⁺ staining of $n = 4$ tumours per indicated genotype. DAPI nuclear staining is in blue; Lgr5 in green. Scale bar, 20 μm . **c**, Per cent Lgr5-GFP⁺ cells in subcutaneous AKVPL and AKVPSL tumours collected

three weeks after implantation (FACS data represented as mean \pm s.d., $n = 5$ tumours per genotype). **d**, Per cent clonogenic cells in AKVPL and AKVPSL organoid cultures estimated with ELDA⁴⁸ ($n = 2$ independent experiment per genotype; error bars represent the 95% confidence interval). **e**, Lgr5-GFP⁺ cell count and fluorescence intensity of *in vitro* organoid cultures with indicated genotype as determined by FACS. * $P < 0.05$, ** $P < 0.01$, *** $P < 0.001$; n represents the number of independent animals.



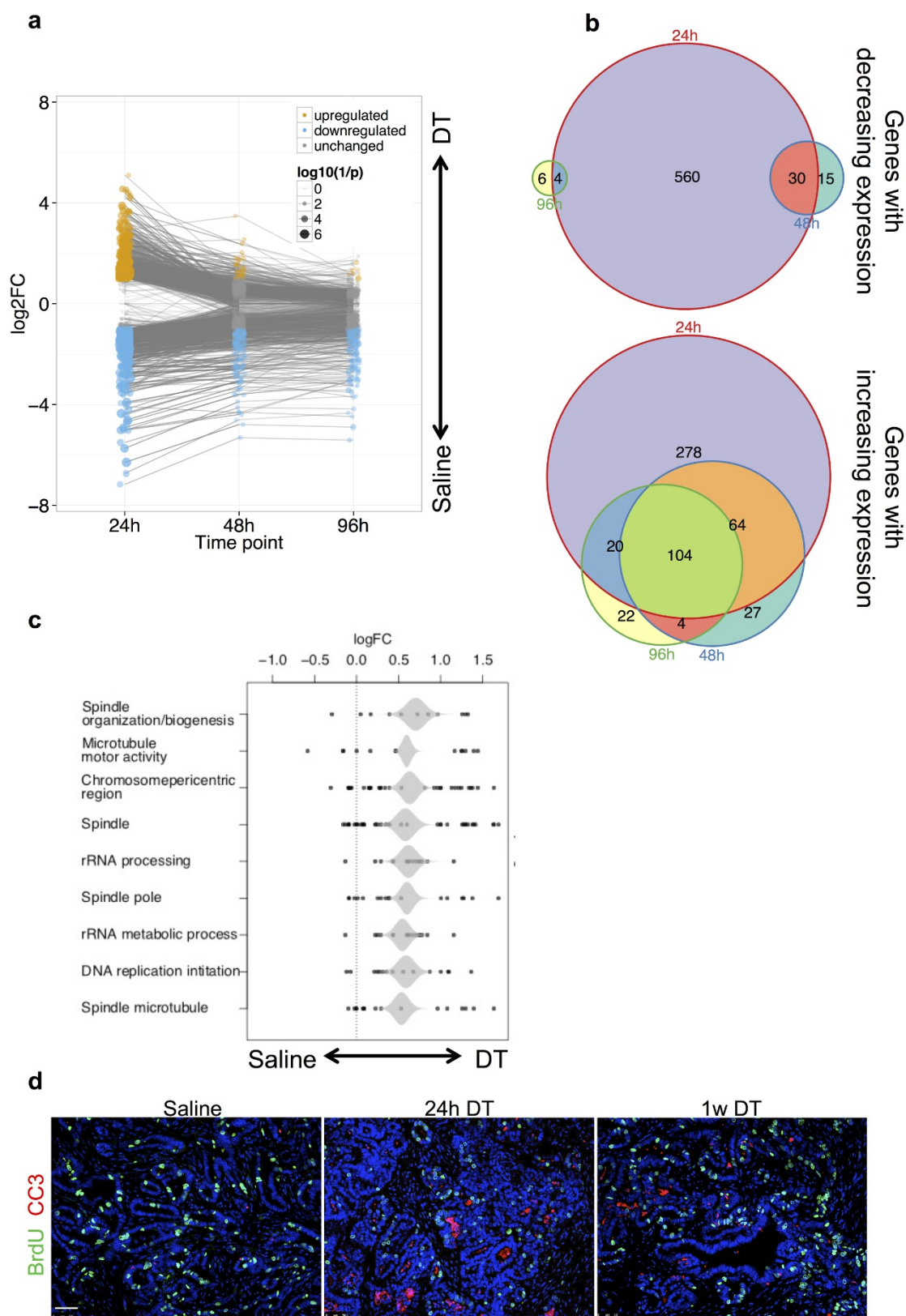
Extended Data Figure 3 | Gene expression analysis and tumorigenic potential of Lgr5⁺ and Lgr5⁻ cells across organoid tumours. **a**, FACS plots for GFP expression in dissociated AKV, AKVPL and AKVPSL tumours. The green and grey gates represent the sorted Lgr5⁺ and Lgr5⁻ populations, respectively. **b**, Heatmap of Lgr5-GFP⁺ and Lgr5-GFP⁻ cells from $n = 4$ AKVPSL tumours for expression of intestinal stem cell (ISC) and canonical Wnt target genes (data are represented as mean-centred RPKM). **c**, QuSAGE of indicated gene signatures in Lgr5-GFP⁺ versus Lgr5-GFP⁻ cells from AKVPSL and AKVPL tumours ($n = 4$ tumours per

genotype). **d**, Tumour-enuftment efficiency of Lgr5⁺ and Lgr5⁻ cells from AKVPL and AKVPSL tumours. **e**, Per cent tumour-initiating cells (TICs) in Lgr5-GFP⁺ and Lgr5-GFP⁻ cell populations from AKVPL and AKVPSL tumours estimated with ELDA⁴⁸ ($n \geq 5$ grafts per dilution; error bars represent the 95% confidence interval). **f**, Per cent GFP⁺ cells in secondary tumours that originated from either 2,500 Lgr5-GFP⁺ or 2,500 Lgr5-GFP⁻ AKVPSL tumour cells ($n = 5$ grafts per cell population). * $P < 0.05$; ** $P < 0.01$; *** $P < 0.001$.



Extended Data Figure 4 | Effects of *Lgr5*⁺ cell depletion on tumour growth. **a, b**, Representative sections of $n = 3$ AKVPL tumours per condition stained for GFP (indicating *Lgr5*, green), cleaved caspase 3 (CC3, red) and nuclei (DAPI, blue). White arrows indicate yellow double positive cells that are detectable as early as 6h after initiation of DT treatment, confirming specific depletion of the *Lgr5*-GFP⁺ cell population. Scale bar, 20 μm. **c, d**, Dosing schedule (c) and tumour

growth (d) of mice with subcutaneous AKVPL allografts in response to intermittent DT treatment ($n = 8$ for the saline- or $n = 7$ for DT-treated group). **e, f**, Dosing schedule (e) and tumour growth (f) of mice with subcutaneous AKVPSL allografts in response to continuous DT treatment ($n = 7$ for each treatment group). n represents the number of independent animals.

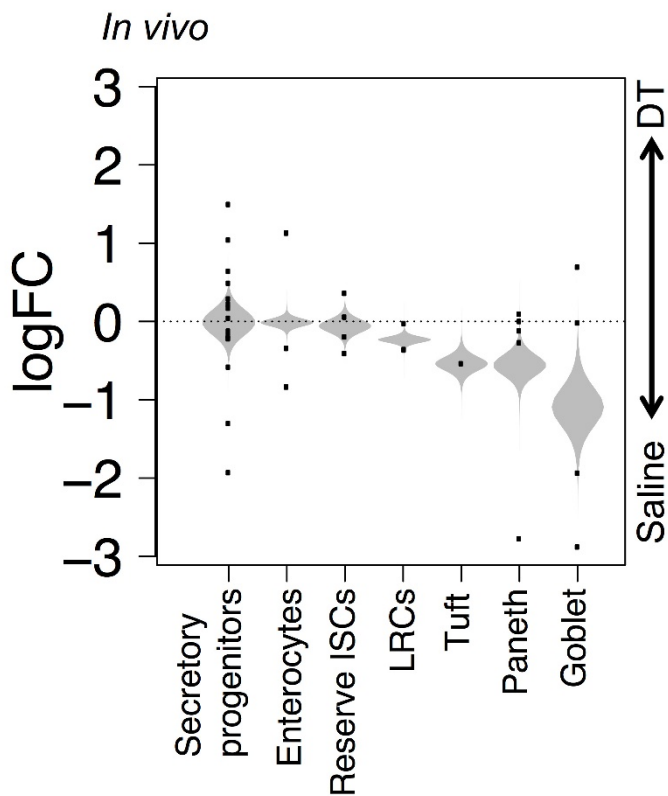


Extended Data Figure 5 | Gene expression profiling of DT-treated tumours. **a**, Gene-expression analysis of bulk AKVPL tumour cells isolated by FACS at different time points after a single dose of either saline or DT ($n = 4$ tumours per time point and condition). **b**, Venn diagram depicting the number of differentially expressed genes for the samples in **a** at various time points after treatment. Number of genes with increasing or decreasing expression patterns are depicted. **c**, QuSAGE of

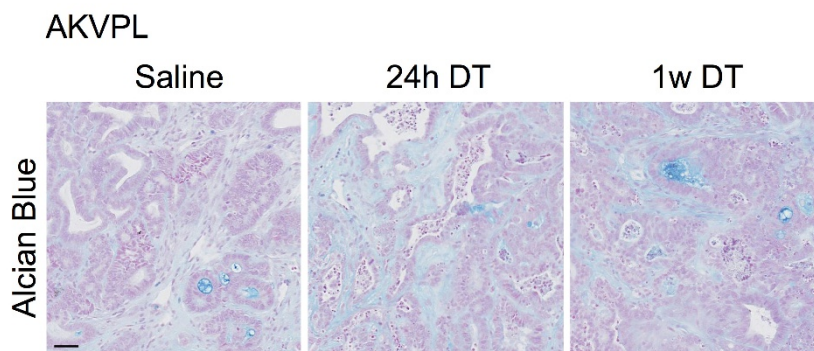
indicated gene signatures in DT- versus saline-treated AKVPL tumours 24 h after treatment. **d**, Representative images of $n = 3$ AKVPL tumours per condition stained for BrdU (green), cleaved caspase 3 (CC3, red) and nuclei (DAPI), revealing dynamic changes in proliferation and cell death after DT treatment for indicated length of time. Scale bar, 50 μm . n represents the number of independent animals.

a

Intestinal cell specific signatures

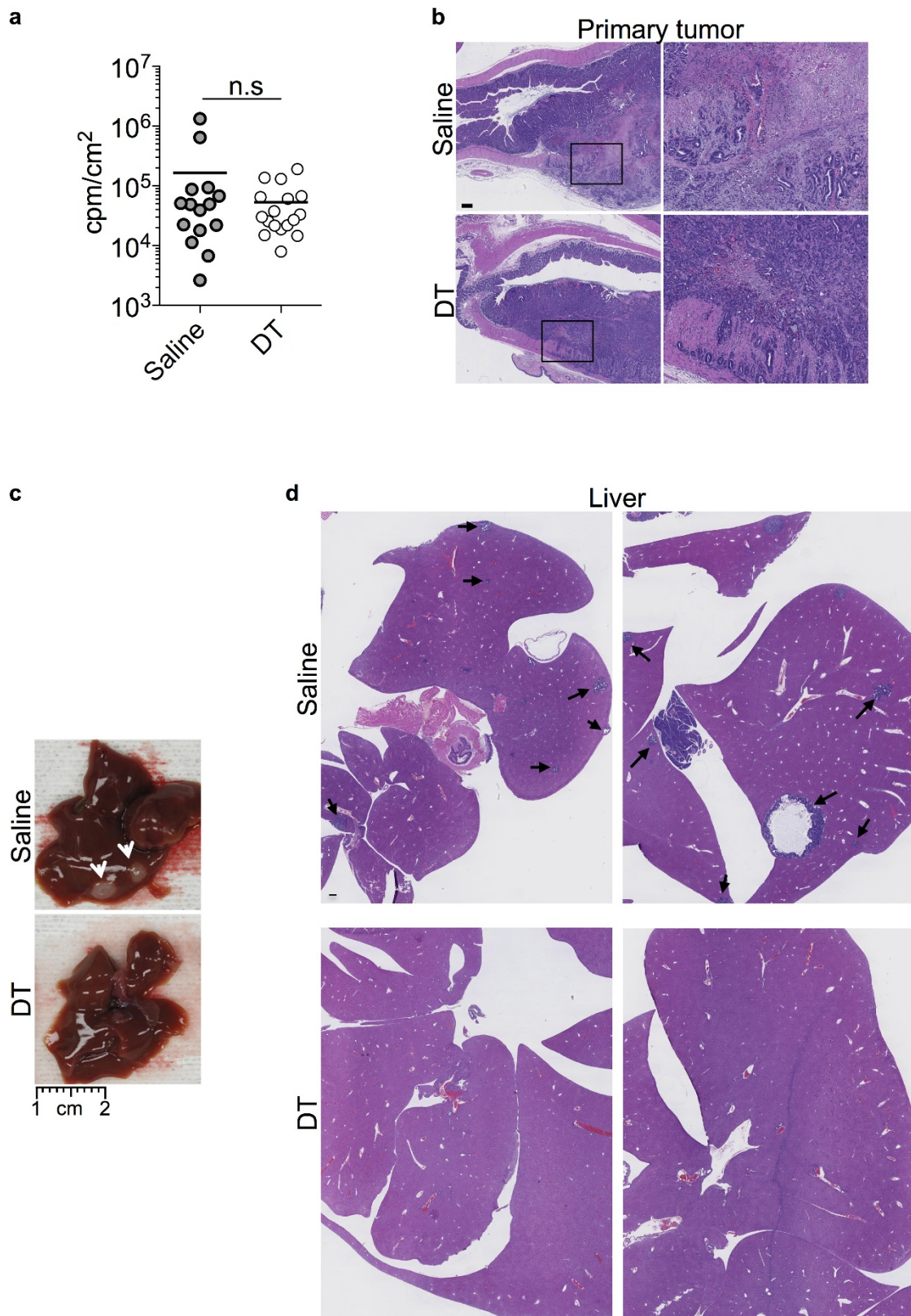


b



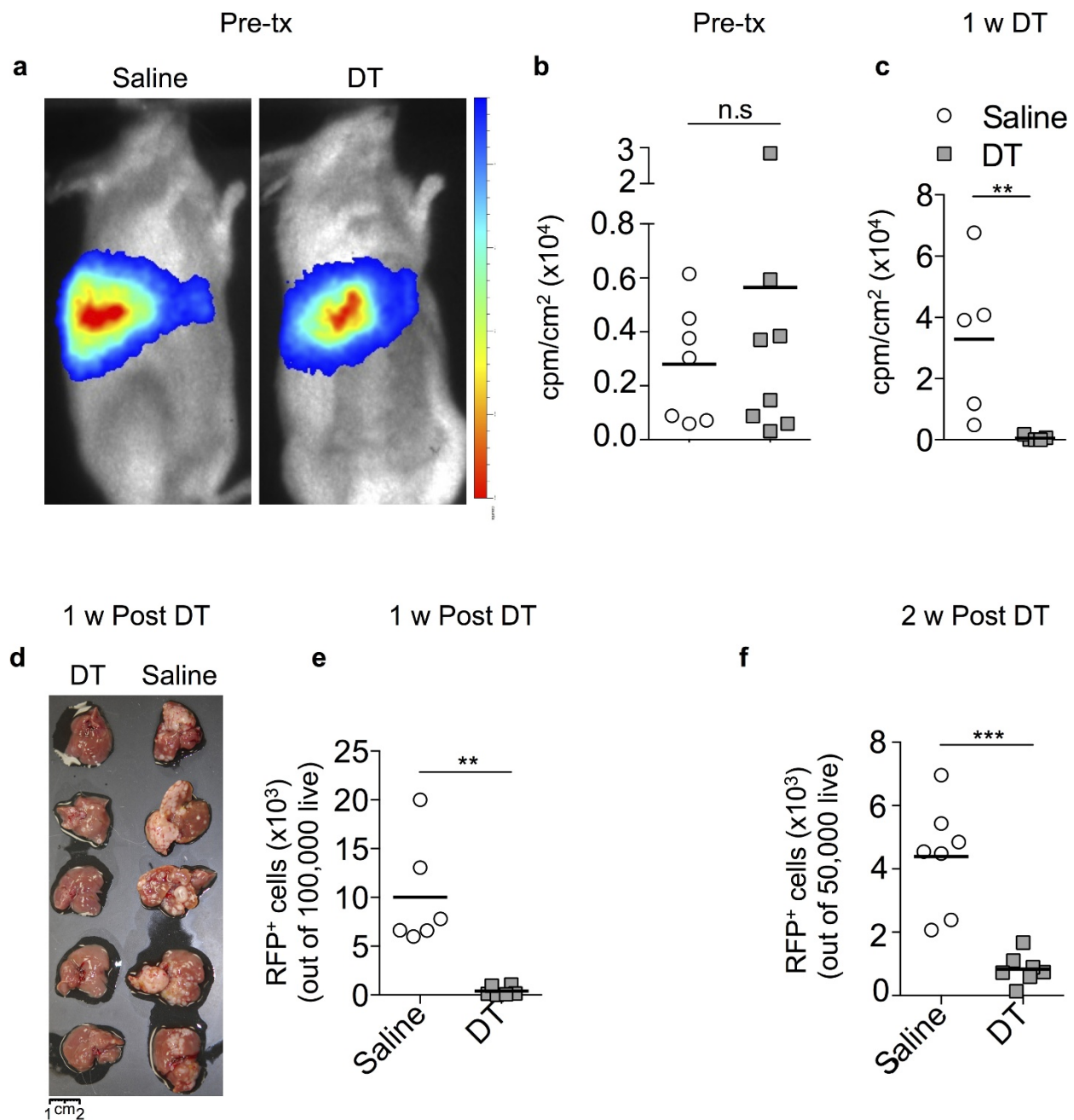
Extended Data Figure 6 | Association of AKVPL tumours with intestinal cell signatures during DT treatment. **a**, QuSAGE of intestinal cell gene signatures²³ in DT- versus saline-treated AKVPL tumours 24 h after treatment. **b**, Representative images of $n = 3$ AKVPL tumours per

condition stained with Alcian blue to evaluate the number of goblet cells after DT treatment for the indicated length of time (counter stained with nuclear fast red). Scale bar, 20 μm . n represents the number of independent animals.



Extended Data Figure 7 | Morphology of orthotopic tumours and liver metastasis after DT treatment. **a**, Quantification of bioluminescence signal in orthotopic AKVPSL tumours from saline- ($n = 17$) and DT-treated ($n = 15$) animals before liver evaluation. Data represented as mean (lines) and individual animals (circles). **b**, Representative images of haematoxylin and eosin staining of orthotopic AKVPSL tumours from $n = 4$ animals per condition after either saline or DT treatment. Boxed areas show invasive front, which is magnified on the right; note that DT treatment did not abrogate tumour invasiveness. **c**, Gross morphology

of representative livers from $n = 4$ animals with orthotopic AKVPSL tumours treated with either saline (top) or DT (bottom). White arrows indicate macro-metastases that are absent from the DT-treated cohort. **d**, Related to Fig. 3j; histological evaluation of livers from saline- and DT-treated mice with an orthotopic AKVPSL tumour. Black arrows indicate metastatic foci that are absent from the DT-treated cohort. Representative images are shown from $n = 6$ per treatment group. Scale bars, 300 μm (**b**, **d**), 2 cm (**c**). n represents the number of independent animals.



Extended Data Figure 8 | Effect of *Lgr5*⁺ cell depletion in established liver metastasis. **a**, Representative bioluminescent images of mice with established liver metastasis before either saline or DT treatment ($n = 7$ for saline and $n = 8$ for DT). Pre-tx, pre-treatment. **b**, Quantification of the bioluminescence signal in animals with established liver metastasis before DT or saline treatment ($n = 7$ for saline- and $n = 8$ for DT-treated group). **c**, Quantification of the bioluminescence signal in animals with established liver metastasis during (1 w DT) DT treatment. **d**, Related to Fig. 4d, e; livers from either saline- or DT-treated animals with established liver

metastasis were collected one week after treatment. **e**, Number of RFP⁺ tumour cells in enzymatically dissociated livers of mice with established metastasis one week after treatment (FACS data represented as mean (lines) and individual animals (circles and squares); $n = 6$ per treatment group). **f**, Number of RFP⁺ tumour cells in enzymatically dissociated livers of mice with established metastasis two weeks after treatment (FACS data represented as mean (lines) and individual animals (circles); $n = 7$ animals per treatment group). * $P < 0.05$; ** $P < 0.01$; *** $P < 0.001$; ns, not significant; n represents the number of independent animals.